CONVECTION INITIATION AND STORM EVOLUTION FORECASTING USING RADAR REFRACTIVITY RETRIEVALS

D. Bodine[1,2,*], P. L. Heinselman[3], B. L. Cheong[2], R. D. Palmer[1,2], and D.Michaud[1,2]

[1] School of Meteorology, The University of Oklahoma, Norman, OK, U.S.A.
[2] Atmospheric Radar Research Center, The University of Oklahoma, Norman, OK, U.S.A
[3] Cooperative Institute of Mesoscale Meteorological Studies (CIMMS), The University of Oklahoma, Norman, OK, U.S.A

1. INTRODUCTION

Recent breakthroughs in retrieving near-surface refractivity from weather radar are providing new opportunities for observing near-surface moisture with very high resolution [Fabry et al., 1997; Fabry, 2004]. Refractivity retrievals attained from the NEXRAD network can provide moisture measurements with very high spatial resolution (as small as 2 km) and temporal resolution (5–10 minutes depending on volume coverage pattern). These measurements provide superior spatial resolution to the Automated Surface Observing System (ASOS), which has an average spacing of 90 km [Koch and Saleeby, 2001].

The absence of small-scale moisture measurements near the surface is a major limitation in forecasting convective precipitation [Emanuel et al., 1995; Dabberdt and Schlatter, 1996; National Research Council, 1998]. Several studies have found that strong moisture gradients play an important role in convection initiation along the dryline [Ziegler et al., 1996; Ziegler and Rasmussen, 1998; Parsons et al., 2000]. Ziegler et al. [1996] suggested that the conventional observation network was insufficient for observing meso-γ scale (2–20 km) variations in moisture along the dryline which are critical for convection initiation. Furthermore, numerical simulations have shown that convection initiation is dependent upon accurate high-resolution moisture measurements [Crook, 1996]. Therefore, high-resolution surface moisture measurements obtained through refractivity retrievals may improve convection initiation forecasts.

Several papers have already shown numerous applications of refractivity data based on Fabry's original radar refractivity algorithm [Fabry et al., 1997; Fabry, 2004]. In initial tests of the algorithm near Montreal, Quebec, Fabry [2004] showed that algorithm could provide accurate near-surface refractivity measurements. The International H_20 Project (IHOP) 2002 experiment in the Oklahoma Panhandle showed the capability of the refractivity algorithm to observe moisture changes associated with cold fronts, outflow boundaries, drylines, boundary layer structures, variations in surface moisture fluxes, and nocturnal moisture boundaries [Weckwerth et al., 2005; Fabry, 2006; Demoz et al., 2006; Buban et al., 2007]. Weckwerth et al. [2005] also showed that radar refractivity data could identify strengthening moisture gradients associated with a dryline before a fine line developed in reflectivity. These experiments have suggested potential benefits of refractivity retrievals to short-term forecasting, and two experiments involving forecaster evaluations followed to evaluate the benefits of refractivity retrievals to short-term forecasting.

The Colorado Refractivity Experiment for H20 Research And Collaborative operational Technology Transfer (REFRACTT) was conducted using four radars in northeast Colorado [Roberts et al., 2008]. The experiment sought to obtain forecaster feedback on the utility of refractivity data from forecasters at the Denver Weather Forecast Office (WFO). In the limited number of responses, forecasters found that the refractivity data were useful for observing moisture changes associated with the Denver Convergence Zone, and providing observations of cold fronts at smaller scales than the current observation network. The forecaster evaluations from REFRACTT were limited by technical issues, so it remained unclear if the benefits of the refractivity algorithm warranted operational retrievals of refractivity into the Advanced Weather Interactive Processing System (AWIPS).

During the KTLX Spring 2007 and 2008 Refractivity Experiments, forecasters evaluated radar refractivity retrievals over two two-month periods and provided 41 surveys evaluating radar refractivity retrievals [Heinselman et al., 2008]. The experiment sought to obtain a comprehensive evaluation of the benefits and limitations of refractivity retrievals, and determine if forecasters thought refractivity should be implemented into AWIPS. Forecasters stated refractivity retrievals increased in confidence in moisture trends and provided observations at smaller scales than standard observations. However, forecasters did not find that refractivity retrievals added significant benefit to their forecasts, as Oklahoma Mesonet data provided sufficient spatial and temporal resolution to identify most mesoscale features. Accordingly, the forecasters gave relatively low importance to implementing refractivity into AWIPS. The study concluded that additional research is needed to identify new applications of refractivity data that provide information to forecasters that cannot be obtained from the current observation network [Heinselman et al., 2008].

* *Corresponding author address:* David Bodine, University of Oklahoma, School of Meteorology, 120 David L. Boren Blvd., Rm 4630, Norman, OK 73072-7307; e-mail: bodine@ou.edu

While previous studies have focused on the general applications of refractivity data, this paper will show several case studies illustrating new refractivity applications that provide information not attainable from the current observation network. This paper will illustrate the capability to use refractivity data to improve convection initiation and storm evolution forecasts by demonstrating the following applications:

- Identifying small-scale moisture pools that reduce convective inhibition
- Detecting boundaries before fine lines develop and assessing moisture changes across boundaries
- Detecting storm outflow and assessing its impact on nearby storms
- Observing rear-flank downdraft and gust front development in supercells

2. RADAR REFRACTIVITY RETRIEVAL ALGORITHM

2.1. Theoretical Foundation

Fabry et al. [1997] and Fabry [2004] developed the framework for radar refractivity retrieval using Doppler radars. The technique uses phase measurements from ground targets to obtain a refractivity field. Since radar phase wraps many times in one range gate, Fabry found that using a phase difference between the current time and a reference time reduced the phase wrapping, thus making the technique feasible. Additional constraints are also required to select the ground targets whose phase varies with changes in the refractive index.

The index of refraction, *n*, is a function of temperature, pressure, and water vapor pressure. The index of refraction near the earths surface is approximately 1.003 and changes in the refractive index are usually very small. The refractive index is often rewritten as refractivity *N* (expressed in N-units) to improve the ease of interpretation [Bean and Dutton, 1968].

$$N = (n-1) \times 10^6 \tag{1}$$

Bean and Dutton [1968] showed that refractivity could be related to temperature, pressure and water vapor pressure using the following equation:

$$N = 77.6\frac{p}{T} + 3.73 \times 10^5 \frac{e}{T^2} \tag{2}$$

where *p* is pressure in millibars, *T* is the temperature in Kelvin, and *e* is the water vapor pressure in millibars. The first term is proportional to air density by the equation of state and the second term is directly proportional to water vapor pressure. The first term is often called the dry term, N_{dry}, and the second term is often called the wet term, N_{wet}. For warmer temperatures, the wet term causes more variation in *N* than the dry term (Fig. 1). Thus, for warmer temperatures, refractivity provides a good approximation for surface moisture, as temperature and pressure changes affect refractivity less than moisture changes. At cooler temperatures, the contribution of temperature must be considered, as the variability of refractivity will be largely due to both temperature and water vapor. Therefore, additional observations may be required for retrieving the water vapor field for cooler temperatures to ensure that refractivity changes are caused by changes in water vapor.

As explained above, changes in atmospheric conditions lead to changes in the refractive index and refractivity. Although the time required for the electromagnetic beam to travel to a target and back is directly proportional to the refractive index, the accuracy of the time measurements is not sufficient to estimate the refractive index. Instead, radar phase must be used, which is related to the refractive index by the following equation

$$\phi = -\frac{4\pi f}{c}\int_0^r n(r')dr' \tag{3}$$

where *f* is the transmitted frequency, *c* is the speed of light, *r* is the range, and ϕ is the phase of the electromagnetic wave. To mitigate phase wrapping, Fabry used two scans to obtain a phase difference instead of a single measurement of phase. The phase difference is calculated using the following equation:

$$\Delta\phi(r) = \phi(r,t_1) - \phi(r,t_0) = -\frac{4\pi f}{c}\int_0^r [n(r',t_1) - n(r',t_0)]dr' \tag{4}$$

where t_1 and t_0 are the two measurement times, t_0 is usually called the reference time. To obtain the refractive index, the range derivative of equation (4) is taken. The resulting equation relates the change in refractive index to the phase difference. Using the relationship between refractivity and the refractive index defined in equation (1), the resulting equation becomes

$$\Delta N = -10^6 \frac{4\pi f}{c}\frac{\partial}{\partial r}[\phi(r,t_1) - \phi(r,t_0)] \tag{5}$$

This equation relates the range derivative of the phase difference between the current scan t_1 and the reference scan t_0 to the refractivity difference between the reference refractivity measurement and the current refractivity measurement.

2.2. Algorithm

The Atmospheric Radar Research Center at the University of Oklahoma has developed an independent algorithm for refractivity retrieval based on the algorithm designed by Fabry et al. [1997]; Fabry [2004]. The algorithm has been

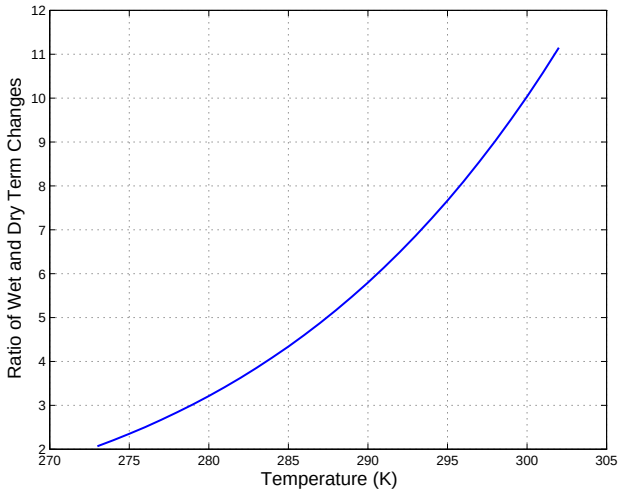

Figure 1: Plot of the ratio of the wet and dry term changes required for a 1 K change in dewpoint temperature (wet term) and temperature (dry term) as a function of temperature, assuming saturation and a constant pressure of 970 mb. For example, at 290 K, the change in refractivity required for a 1 K increase in dewpoint temperature is approximately 6 times greater than the change in refractivity required for a 1 K change in temperature.

adapted for different weather radars, including the WSR-88Ds, Collaborative Adaptive Sensing of the Atmosphere (CASA) X-Band Radars, and the National Weather Radar Testbed (NWRT) Phased Array Radar (PAR). Cheong et al. [2008] provides a detailed description of the University of Oklahoma refractivity algorithm, although it will be described briefly here.

Before refractivity retrievals can be made, a reference map of phase and refractivity must be obtained. The first set of phase measurements are called the reference phase, made at time t_0. The reference phase measurements must be made when the refractivity field is nearly uniform and is not changing with time. Thus, when the refractivity field is constant, the ground clutter target's phase should also be constant if the target's phase is only changing due to refractivity. A reference refractivity map, N_{ref} is also produced at the same time, t_0. While Fabry's technique assumes the reference refractivity map was homogenous, the OU algorithm uses data from the Oklahoma Mesonet to calculate refractivity and then objectively analyzes the Mesonet refractivity data to produce a reference refractivity map.

After the reference maps have been produced, phase measurements are made at scan time t_1. A phase difference is calculated between the measured phase at t_1 and the reference phase at t_0. A masking procedure censors poor clutter targets based on two indices — the quality index (QI) and reliability index (RI). The quality index is calculated for the phase measurements at t_1. The quality clutter targets have high signal-to-noise ratios, narrow spectrum width and near-zero radial velocities. If the clutter targets exhibit these characteristics, then the target's QI will be high. The reliability index is calculated for the reference phase measurements and is based on the variations of the target's phase with time (over an hour or two). When the refractivity field is nearly constant, a quality clutter target's phase should exhibit minimal temporal variations. Thus, the quality clutter targets will have a high RI. Finally, based on set threshold values of the QI and RI, any phase measurement with a QI or RI below the threshold value is censored.

Spatial filtering of the phase data is required to obtain a smoothed field because the quality targets are distributed unevenly and sparsely. A linear gradient of the phase difference field is calculated by taking the mean of the phase differences between all uncensored radially adjacent gates. The refractivity field will usually have a mean value shifted from the reference refractivity field, which causes a linear gradient in phase difference. The linear gradient is subtracted from the phase differences to produce a perturbation component. The perturbation component is subsequently smoothed using two separate convolutions with a fixed smoothing window. The first convolution smoothes the data along each azimuth and the second convolution smoothes the data along each radial. After the phase difference field has been smoothed, the linear gradient in phase difference is added back to the smoothed phase field.

The final step in the algorithm is calculating the range derivative of the smoothed phase difference field to obtain the refractivity difference, ΔN. By adding the refractivity difference to the reference refractivity measurement, N_{ref}, an absolute refractivity field can be obtained [Cheong et al., 2008]. In addition to absolute refractivity fields, scan-to-scan refractivity change fields (hereafter called scan-to-scan refractivity) are produced by substituting the phase measurements from the preceding volume scan for the reference phase measurements. Given the uncertainty of the reference refractivity field, scan-to-scan refractivity measurements are more accurate than absolute refractivity measurements because the reference scan is eliminated [Fabry, 2004].

2.3. Limitations

In relatively flat terrain, the range of refractivity retrievals is typically limited to approximately 50 km because of earth curvature effects. Within the 50-km range, there are a limited number of quality targets that exceed the threshold values of QI and RI. The noisiness of the data also requires spatial filtering, which reduces the spatial resolution of the refractivity data to 2 km. The coverage of clutter targets is generally better in urban areas where the density of quality clutter targets is higher.

Another limitation of the refractivity algorithm is that the range derivative of the phase difference field is not always well represented by a linear gradient. According to equation (1), a linear gradient represents the mean of the change of the refractivity field from the reference refractivity measurement ($\overline{N - N_{ref}}$). Thus, strong spatial gradients in refractivity will produce a complex field of the perturbation component of the phase difference. In regions with poor clutter coverage, the sparseness of the phase measurements may not be sufficient to measure the complex perturbation component of the phase difference, thus hindering refractivity measurements with strong refractivity gradients. The Atmospheric Radar Research Center is currently working on methods for improving estimation of the mean gradient for nonlinear phase gradients.

The reference map also limits the accuracy of the absolute refractivity retrieval because the reference refractivity measurement must be accurate. There are usually temporal and spatial variations of refractivity, which limits the opportunities to create a good reference map. Because the radar phase wraps, the estimate of the mean gradient of the phase difference has a limited unambiguous value. In terms of the refractivity difference, the unambiguous refractivity range [Cheong et al., 2008] is defined by

$$\Delta \mathrm{N_a} = \pm 10^6 \frac{c}{4\mathrm{f}\Delta \mathrm{r}} \tag{6}$$

ΔN_a is approximately 100 N-Units for the WSR-88Ds and the NWRT PAR and 83 N-Units for the CASA X-Band Radars. Thus, the reference map should be created when the range of refractivity values will encompass all of the expected refractivity values for the period of operation. Otherwise, it may be necessary to shift the reference map or create a new reference map if the refractivity values exceed the unambiguous refractivity range of radar. Recent studies have also shown that the bias and standard deviation increase with time from the reference measurement. Thus, reference maps must be updated regularly to avoid introducing bias or random errors.

3. CONVECTION INITIATION CASE STUDIES

The refractivity data used in this study were collected during the KTLX Spring 2007 and 2008 Refractivity Experiments. Refractivity data were collected from 8 April 2007 to 10 July 2007 on the Oklahoma City WSR-88D (KTLX), and from 20 February 2008 to 20 May 2008. Throughout the experiment, refractivity data were compared with the Oklahoma Mesonet stations within the refractivity domain. The Oklahoma Mesonet provides 5-minute surface observations with approximately 35 km station spacing [Brock et al., 1995; McPherson et al., 2007]. The Mesonet data also provided verification of the accuracy of the refractivity data, and helped resolve ambiguities about the contributions of the dry and wet terms in cool season cases.

After the experiment, a climatology of a variety of meteorological phenomena observed by refractivity was produced. Table 1 shows the number of refractivity cases for different phenomena during the span of this study. Outflow and moisture boundaries were the most commonly observed phenomena, and were most easily observed in the scan-to-scan refractivity change field. Four cases were identified where refractivity data captured a phenomena that contributed to convection initiation. During the experiment, drylines did not mix far enough east to be frequently observed by KTLX, resulting in relatively few dryline cases. In addition to these cases, the refractivity data captured the evolution of the boundary layer and subtle differences in moisture fluxes between urban and rural areas on a daily basis.

3.1. Convection initiation with small-scale moisture pool

In the absence of strong forcing, small-scale changes in thermodynamics or dynamics may explain why storms form at a particular location. Convective inhibition (CIN) is defined as a negatively buoyant layer that can suppress convection until CIN is reduced by thermodynamic and dynamic changes (e.g. increasing moisture or lift). By increasing

Table 1: Observed KTLX refractivity cases for meteorological phenomena between 8 April 2007 to 10 July 2007 and 20 February 2008 through 20 May 2008.

Phenomena	Number of Refractivity Cases
Outflow/Moisture boundary	32
Cold Front	14
Dryline	5
Moisture advection	3
Convection initiation	4
Storm outflow	3

the temperature or dewpoint temperature of a parcel, the parcel becomes less dense and more buoyant, leading to a decrease in CIN. Similarly, a local increase in lift will increase the parcel's vertical acceleration and effectively decrease CIN by generating more parcel momentum. Refractivity data provide the resolution needed to observe the small-scale changes in moisture that are sometimes critical for convection initiation.

The impact of small-scale variability of moisture on the development of an isolated storm was analyzed using refractivity, Rapid Update Cycle (RUC) analyses and Mesonet data. When this isolated storm developed, a weak squall line was developing in south central Oklahoma (Fig. 2), with some stratiform precipitation in southwest Oklahoma. The RUC analysis showed between 0 and 20 J kg^{-1} of CIN in the region where the isolated storm and squall line developed. At upper-levels, the 500-hPa trough axis was located over southeast New Mexico, making this region a favorable environment for weak upward motion. The RUC reanalysis from 1800 UTC showed vertical velocities at 500 hPa between 0 to 5 cm s^{-1} where the isolated storm developed, and vertical velocities greater than 30 cm s^{-1} where the squall line was developed. To confirm the RUC vertical velocity analysis, 10-m wind observations from the Oklahoma Mesonet were used to compute surface convergence. At 1800 UTC, the computed surface convergence near the squall line was 4×10^{-4} s^{-1} compared to 1×10^{-4} s^{-1} where the isolated storm developed, thus implying greater positive vertical velocities near the squall line and confirming the RUC analysis. Since the isolated storm developed in a region with comparatively weak lift and weaker ensuing positive vertical velocities, additional thermodynamic or dynamic changes must have occurred to allow convection initiation of the isolated storm.

Prior to the development of the isolated storm, a moisture pool characterized by a positive anomaly in scan-to-scan refractivity developed (Fig. 3bi-biv). The western edge of the moisture pool passed over the Norman Mesonet station between 1726 and 1745 UTC and increased the dewpoint temperature from 16 to 17°C (Fig. 3ai-aii). The winds at the Norman Mesonet station veered slightly to the southwest as the moisture pool passed, locally enhancing convergence at the moisture pool. The dewpoint temperature also increased 1.2°C and 0.9°C at the Oklahoma City East (OKCE) and Spencer (SPEN) Mesonet sites, respectively, as the moisture pool passed. The three Mesonet stations affected by the moisture pool had an average observed change in dewpoint temperature of 1.0°C. The maximum change in radar refractivity associated with the moisture pool was approximately 10 N-units, which corresponds to a 2°C increase in dewpoint temperature assuming constant temperature and pressure.

To investigate the effects of a moisture pool on convection initiation, the 0000 UTC 1 May 2007 OUN (Norman, Oklahoma) sounding and the 1800 UTC 30 April 2007 LMT (Lamont, Oklahoma) soundings were modified using NSHARP [Hart and Korotky, 1991]. The thermodynamic profile of the 1800 UTC LMT was closest to the 1700 UTC RUC sounding analysis for Norman, Oklahoma. However, since the LMT sounding was 180 km from the location of convection initiation, the OUN sounding will still be included. The original soundings were modified to represent the average surface conditions from Mesonet stations within the refractivity domain at the time of convection initiation (Scenario 1). Then, a set of new soundings were produced by introducing a moisture perturbation, similar to observed changes associated with the moisture pool.

Based on the observed moisture changes at the Mesonet stations and the calculated changes in refractivity, two new scenarios were created. Scenario 2 includes a 1°C dewpoint temperature increase based on the average Mesonet dewpoint temperature change associated with the moisture pool. Scenario 3 investigates a 2°C increase in dewpoint temperature based on the maximum observed radar refractivity change. Given that the Mesonet has coarser spatial sampling and the moisture pool did not pass directly over a Mesonet station, the Mesonet likely underestimated the maximum change in dewpoint temperature. The LMT 1800 UTC and OUN 0000 UTC

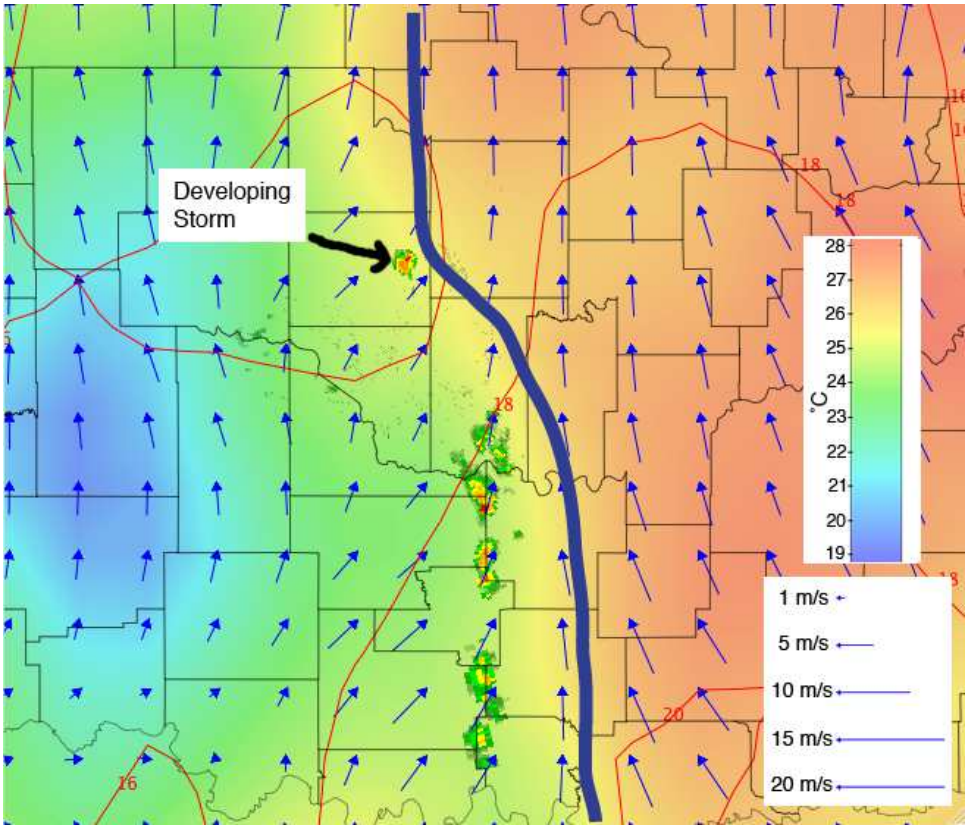

Figure 2: Reflectivity (3.5°tilt), surface wind ($m\,s^{-1}$), temperature (shaded) and dewpoint temperature (contoured in red) at 1815 UTC 30 April 2007. The differential heating boundary is marked by the blue line.

Table 2: Thermodynamic variables from modified sounding analyses for the OUN 0000 UTC sounding on 1 May 2007. Scenario 1 used the mean surface conditions from the Mesonet prior to convection initiation. Scenario 2 and 3 included a 1 and 2°C dewpoint temperature increase, respectively.

Case	T (C)	Td (C)	CIN (Jkg^{-1})	SBCAPE (Jkg^{-1})	LFC (m)	LCL (m)
Scenario 1	25	15	-14	501	2001	1383
Scenario 2	25	16	-4	1018	1719	1259
Scenario 3	25	17	0	1548	1240	1111

Table 3: Thermodynamic variables from modified soundings analyses for the LMT 1800 UTC sounding on 30 April 2007. Scenario 1 used the mean surface conditions from the Mesonet prior to convection initiation. Scenario 2 and 3 included a 1 and 2°C dewpoint temperature increase, respectively.

Case	T (C)	Td (C)	CIN (Jkg^{-1})	SBCAPE (Jkg^{-1})	LFC (m AGL)	LCL (m AGL)
Scenario 1	25	15	-22	408	2319	1371
Scenario 2	25	16	-5	852	2045	1223
Scenario 3	25	17	0	1380	1124	1124

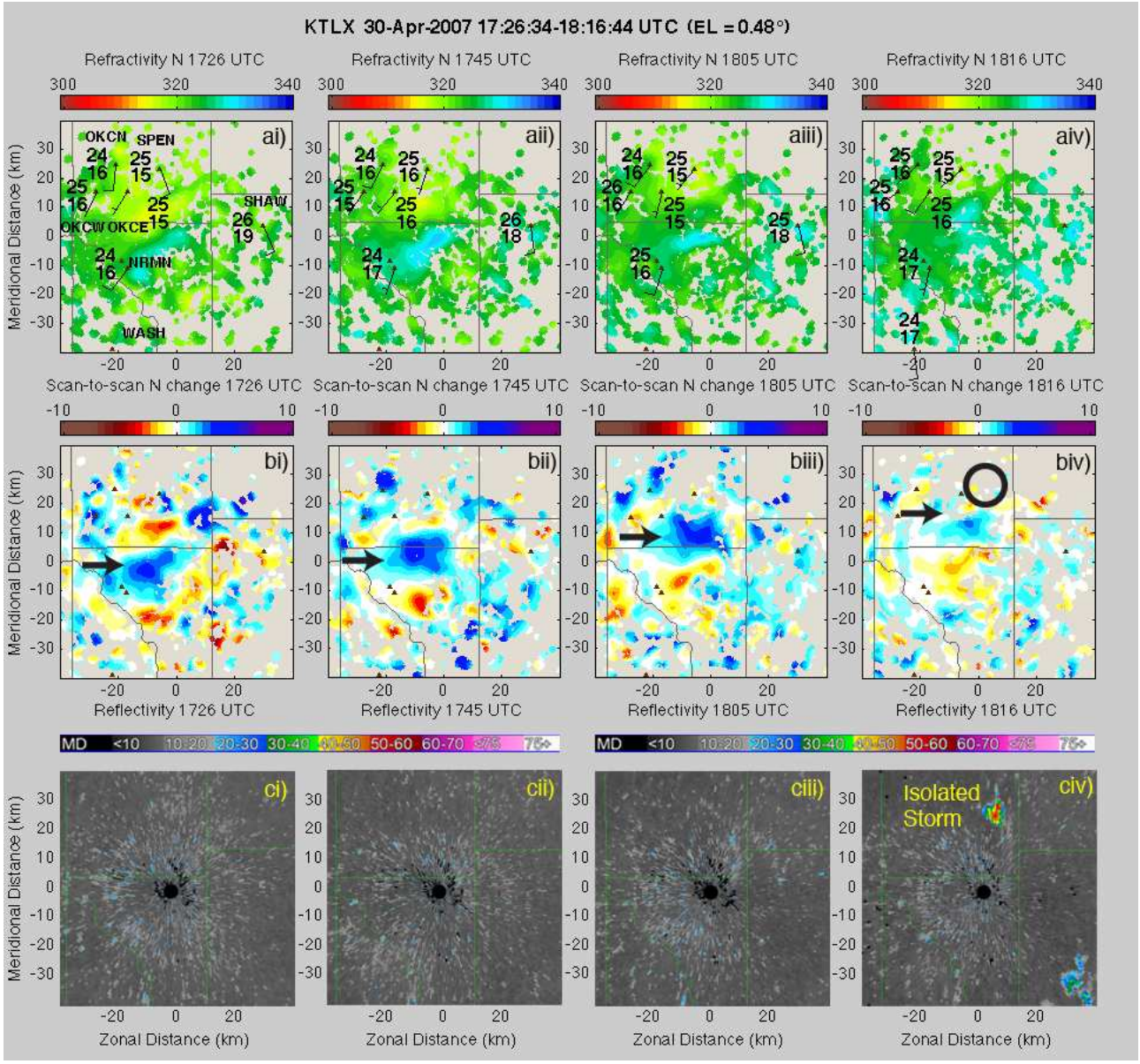

Figure 3: a) Refractivity, b) scan-to-scan refractivity change, and c) 0.5° tilt reflectivity at 1726, 1745, 1805, and 1816 UTC 30 April 2007. The black arrow denotes the position of the cell in the scan-to-scan refractivity and the position of the storm at 1816 UTC is shown by black circle in reflectivity.

soundings were modified based on Scenarios 2 and 3, using the surface conditions listed in Tables 2 and 3.

The modified sounding analyses at both OUN and LMT showed that the thermodynamic changes associated with the moisture pool supported convection initiation by substantially weakening the remaining convective inhibition, significantly increasing surface-based convective available potential energy (SBCAPE), and lowering the level of free convection. For a 1°C increase in dewpoint temperature (scenario 2), convective inhibition was reduced from -14 and -22 to -4 and -5 J kg^{-1} for soundings OUN and LMT soundings, respectively (Tables 2 and 3). The increases in moisture also lowered the LFC heights, increasing the likelihood of surface-based convection initiation with relatively weaker lift. Scenario 2 also doubled the SBCAPE for both the OUN and LMT soundings. The 2°C increase in dewpoint temperature (Scenario 3) expunged CIN, reduced LFC height by a factor of 2, and tripled SBCAPE for both the OUN and LMT soundings. Based on this analysis, it is likely that the initiation of the isolated storm depended on small-scale variations in moisture, and significant changes in the storm's intensity could result from small-scale variations in moisture.

In summary, the sounding analyses showed that convection initiation was not likely without modifying the surface conditions or lifting the parcel above the level of free convection. The modified surface conditions, based on the observed changes in refractivity from the Mesonet and the radar, significantly reduced the CIN and would have likely enabled thunderstorm development. Hence, the thunderstorm was probably caused by the locally enhanced thermodynamics of the moisture pool rather than large-scale forcing whereas the squall line was forced by a differential heating boundary. Furthermore, the moisture pool observed in refractivity would explain why the thunderstorm developed in that particular location, even though the mean environmental surface conditions were not conducive for convection initiation. The results suggest that refractivity data could be used to produce CIN fields to help forecasters identify small-scale areas that are favorable for convection initiation and CAPE fields to aid storm intensity forecasts.

3.2. Dryline convection initiation

The 21 April 2008 convection initiation event highlighted important processes involved in convection initiation and demonstrated another use of refractivity in convection initiation forecasting and boundary identification and tracking. An isolated supercell developed in Central Oklahoma along the dryline and eventually produced 5.7-cm hail near Paoli, Oklahoma. Prior to convection initiation, confluent flow strengthened the dryline, leading to an increase in moisture convergence and the development of a cumulus field along the dryline. The increasing moisture gradient was evident in refractivity by 1959 UTC (Fig. 4ai), with a maximum refractivity gradient of 0.24 N-units km^{-1}. At this time, the reflectivity data did not show a fine line (Fig. 4ci). By 2215 UTC, the moisture gradient sharpened, characterized by a maximum refractivity gradient of 0.67 N-units km^{-1} (Fig. 4aii). The scan-to-scan refractivity field also showed the moistening behind the moisture boundary as it moved westward (Fig. 4bii).

At 2215 UTC, the first fine line developed two hours after the initial refractivity gradient was observed (Fig. 4cii), in the same location as depicted in refractivity and scan-to-scan refractivity. By 2244 UTC, the fine line was much better defined (Fig. 4ciii). Scan-to-scan refractivity change also clearly showed the position of the boundary, and the maximum scan-to-scan refractivity change observed was 7.1 N-units over 10 minutes (Fig. 4biii). The refractivity field was primarily homogeneous behind the moisture boundary with dewpoint temperatures of 19°C and absolute refractivity of approximately 335 N-units (Fig. 4aiii). As the moisture boundary passed, the six Mesonet stations west of KTLX showed an average increase in dewpoint temperature of 3.3°C and a 31°counter-clockwise change in wind direction. The Shawnee Mesonet station did not show a clear change in dewpoint temperature or wind direction, which suggests the moisture boundary developed within the refractivity domain west of the Shawnee Mesonet station.

Convection initiation occurred (defined by first echo $>$30 dBZ) at 0035 UTC, 74 km southwest of KTLX (Fig. 4civ). Increased lift associated with the boundary collision was indicated by an increase in surface convergence from 0.75×10^{-4} to 2.5×10^{-4} s^{-1} between 2300 and 0000 UTC. The 0000 UTC 22 April 2008 sounding was analyzed using NSHARP to study the impact of the moisture boundary on the thermodynamic profile. Convection initiation occurred closest to the Washington Mesonet station, so the sounding was modified using surface observations from the Washington Mesonet. The analysis showed that the moisture changes associated with the boundary passage caused CIN to decrease from -13 to -1 J kg^{-1}. Thus, the moisture boundary likely contributed to convection initiation through surface moisture changes which led to a reduction in CIN and a lowering of the LFC, and through increased lift associated with the boundary collision. Wilson and Schreiber [1986] found that boundary collisions initiated convection for 84% of 49 colliding boundary cases studied.

Wilson and Schreiber [1986] found that fine lines associated with boundaries often precede convection initiation, thus early detection of the moisture gradient and tracking the boundary would be critical for forecasting the timing of convection initiation for this case. The refractivity data showed an initial refractivity gradient two hours prior to fine line development, and captured the evolution of the

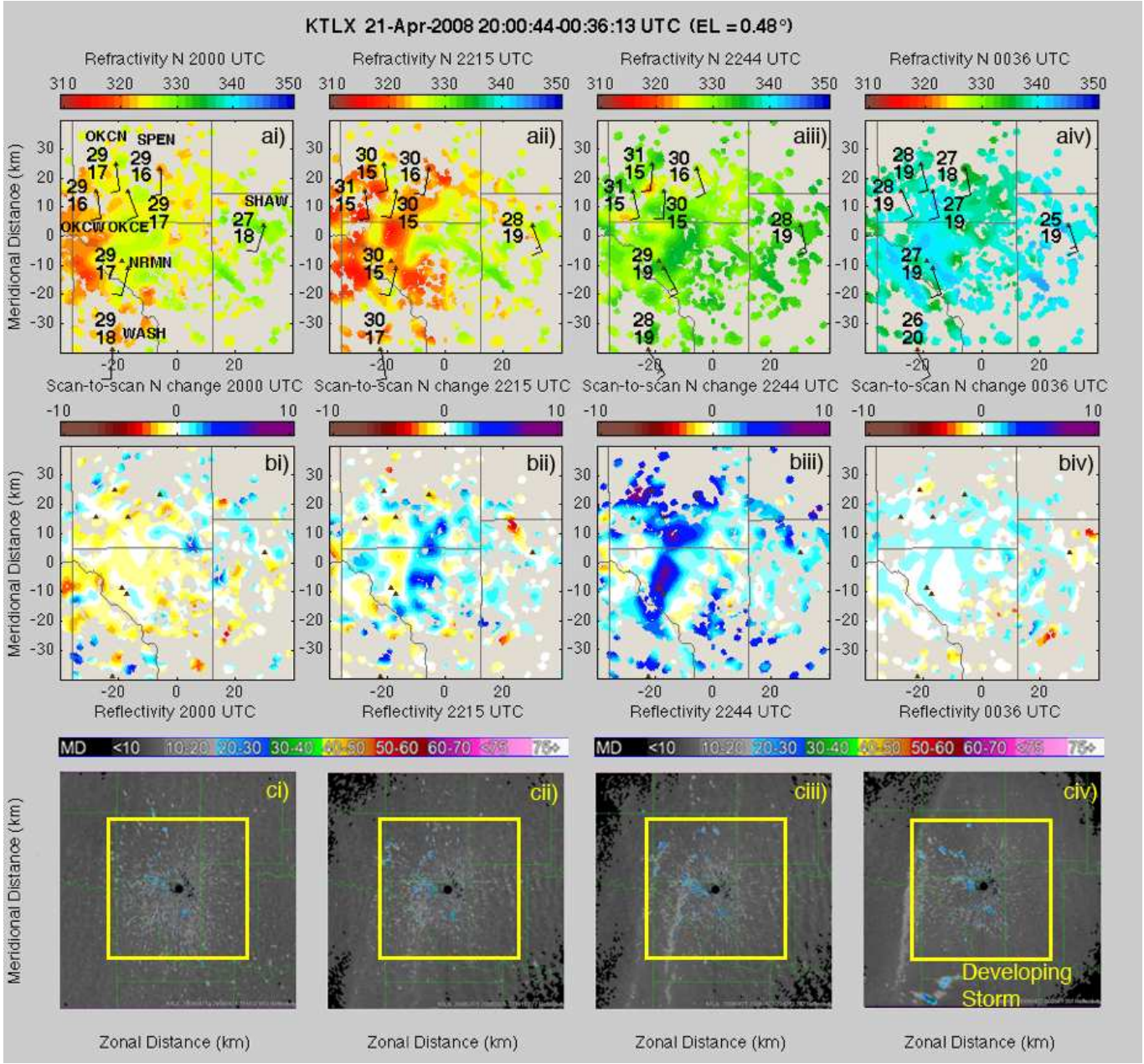

Figure 4: a) Refractivity, b) scan-to-scan refractivity change, and c) 0.5° tilt reflectivity at 2000, 2215, 2244, and 0036 UTC 21 April 2008. The square shows the 80-km wide area depicted in the refractivity and scan-to-scan refractivity.

moisture boundary as the refractivity gradient increased. While boundary detection using reflectivity requires tracers (e.g. insects) to accumulate along convergence lines, refractivity data shows thermodynamic differences across the boundary instantaneously [Weckwerth et al., 2005]. Short-term forecasts of convection initiation could be improved using refractivity data by detecting boundaries sooner and providing more information about the magnitude of moisture changes. The moisture changes across the boundary could be used to estimate the likelihood of convection initiation by reanalyzing soundings. Although convection initiation occurred approximately 34 km outside the refractivity domain, a forecaster could observe the westward moving boundary in refractivity and issue a short-term forecast for an increased likelihood of convection initiation along the dryline. Using a network of radars, the refractivity domain could be expanded and increase the utility of refractivity data for boundary tracking.

4. STORM EVOLUTION AND STRUCTURE CASE STUDIES

4.1. Impact of storm outflow

The refractivity data were not only useful for the convection initiation forecast for the 21 April 2008 supercell (Section 3b), but also demonstrated important applications in nowcasting the evolution of the supercell and its multiple splitting storms. After the supercell developed, the supercell split in McClain County at 0133 UTC on 22 April 2008 (not shown). The right-moving supercell (denoted as storm A) moved eastward along the McClain/Garvin County border while the left-moving supercell moved northeast. At 0145 UTC, the left-moving supercell split, with the left-moving supercell (denoted as storm C) becoming the most intense, even though the environmental shear favored the right-moving supercell. The right-moving supercell (denoted as storm B) collapsed at 0205 UTC.

The refractivity data showed the evolution of the outflow from storm B and its interaction with the storm C. In the 15-min refractivity change at 0205 UTC, a region of positive refractivity was observed surrounding storm B, which indicates cold, moist outflow from the storm B (Fig. 5bi). By 0220 UTC, the 15-minute refractivity change field (Fig. 5bii) showed the leading edge of the outflow from storm B advancing toward storm C. The expansion of the thunderstorm outflow was also evident in the refractivity field, as refractivity increased as the outflow propagated through the southeast quadrant of the refractivity field (Fig. 5aiii). By 0250 UTC, storm C had collapsed as the outflow from storm B reached the storm (Fig. 5civ).

The configuration of these outflow boundaries suggests that the outflow from storm B likely cutoff the inflow of warm, moist environmental air into the supercell, causing storm C to collapse. This mechanism for storm collapse is described in Lemon and Doswell III [1979], which found that a thunderstorm's outflow can disrupt the inflow of warm, moist air into itself or inflow into surrounding thunderstorms. Although storm C was moving into a more stable environment, the environment was still unstable, with between 1000 and 2000 J kg^{-1} of SBCAPE, which would otherwise allow the thunderstorms to continue. Thus, for this case, monitoring outflow boundaries would be critical for nowcasting the collapse of storm C. Storm A also collapsed shortly after storm C, thus it is likely that the outflow from storm B also cutoff storm A's inflow. Unfortunately, this assertion cannot be confirmed using refractivity data because storm A was outside of the refractivity domain.

Convergence lines are often observed along outflow boundaries. However, no convergence lines were observed in reflectivity along the outflow boundary for this case, possibly because the convergence along the leading edge of the outflow boundary may not have been sufficient for a convergence line to develop in reflectivity. Thus, reflectivity would not have been useful for forecasting the collapse of the nearby storms. Furthermore, the high spatial and temporal resolution provided by the refractivity data allowed the storm's outflow to be detected immediately. The outflow was not evident in the Mesonet data until the storms had collapsed because the closest Mesonet station was approximately 20 km away. Furthermore, the area affected by the storm's outflow will be resolved much better by the 2-km resolution of refractivity compared to the 35-km resolution of the Mesonet.

4.2. Supercell observations and tornadogenesis forecasting potential

The thermodynamic characteristics of the rear-flank downdraft (RFD) have important implications on tornadogenesis. Markowski et al. [2002] found that smaller differences in equivalent potential temperature θ_e and virtual potential temperature θ_v between the RFD and the environment increased the likelihood of tornadogenesis and the intensity and duration of the tornadoes. The warm RFDs (smaller difference in θ_e) produce stronger tornadoes than cool RFDs (larger difference in θ_e) because the warm RFDs have greater buoyancy and increase low-level convergence. Furthermore, Markowski et al. [2002] found that high boundary layer relative humidities produce more buoyant RFDs and increase the likelihood of tornadogenesis.

Markowski et al. [2002] speculated that high-resolution, surface thermodynamic measurements are one of the most critical measurements for improving scientific understanding of tornadogenesis. Radar refractivity measurements provide high-resolution near-surface measurements of moisture.

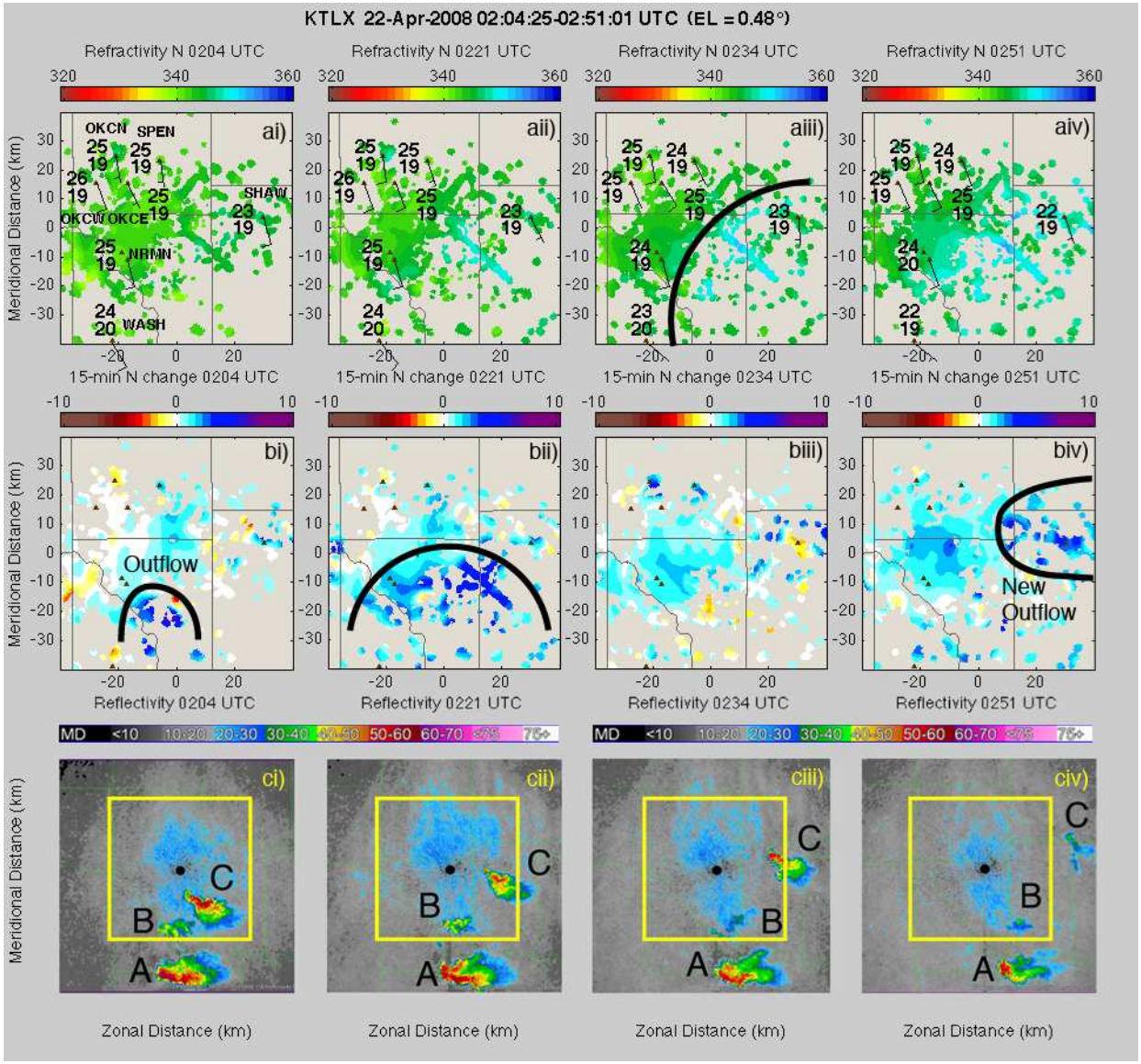

Figure 5: Refractivity a), 15-minute refractivity change b), and 0.5°tilt reflectivity c) at 0204, 0221, 0234, and 0251 UTC 22 April 2008. The square shows the 80-km wide area depicted in the refractivity and 15-minute refractivity change fields. The individual storms are labelled A, B, and C as described in the text. In the 15-minute refractivity change field, the black lines show the areas affected by the outflow from storm B.

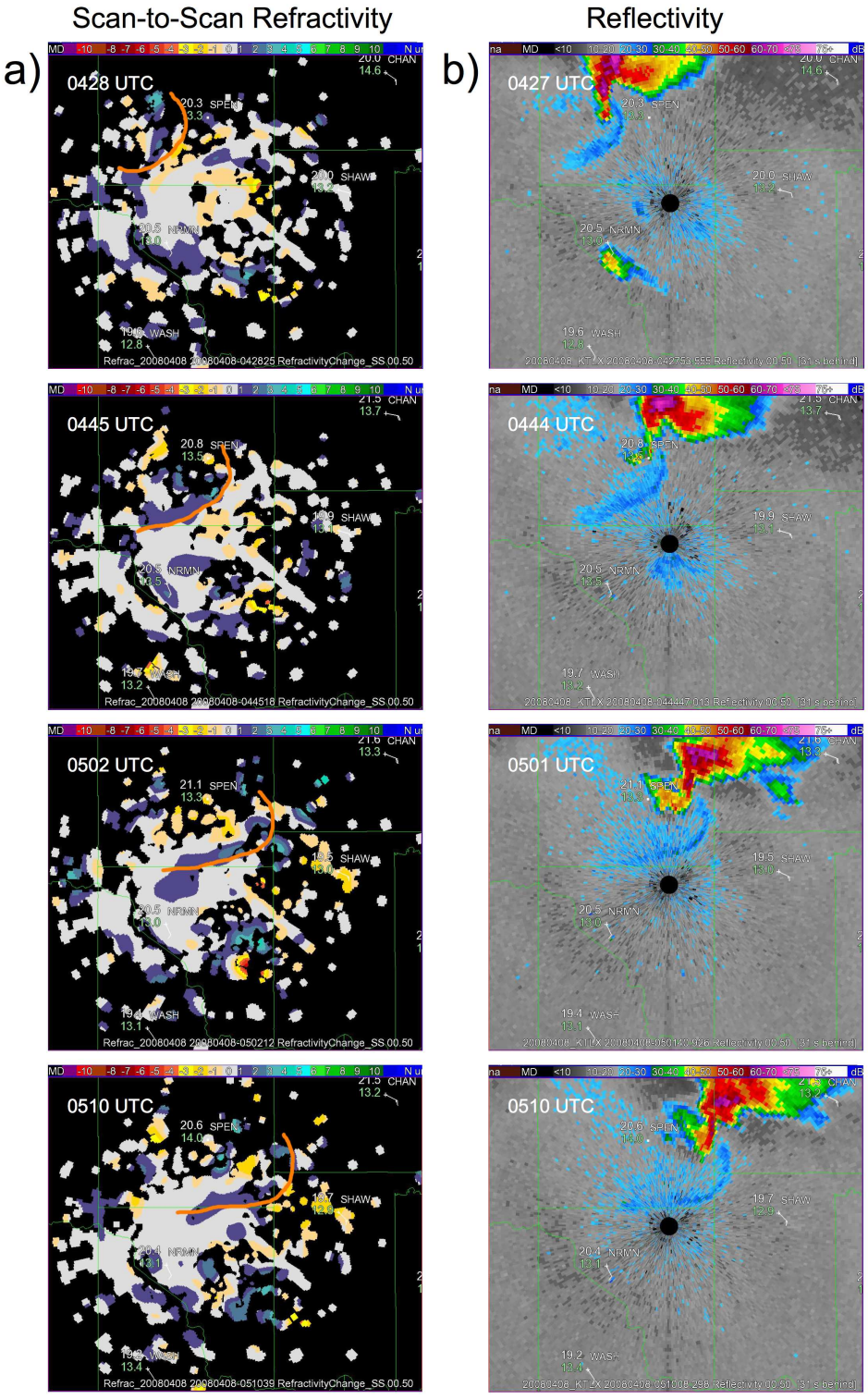

Figure 6: a) Scan-to-scan refractivity change, and b) 0.5° tilt reflectivity at 0428, 0445, 0502, and 0510 UTC 8 April 2008. The orange line shows the position of the gust front in reflectivity.

Given the difficulty in separating the dry and wet refractivity terms, quantitatively analyzing the rear-flank downdraft in terms of virtual potential temperature or equivalent potential temperature would be impossible without a temperature or water vapor measurement. However, refractivity measurements could distinguish between moist and dry RFDs by comparing refractivity measurements within the RFD and the environment. Discriminating between tornadic and nontornadic RFDs by assessing the buoyancy contribution of moisture is one potential forecasting application of refractivity data. The refractivity data could be used in conjunction with microphysical properties of the RFD observed with dual-polarization radar to provide additional information about the buoyancy of the RFD. To determine what refractivity signature would discriminate between tornadic and nontornadic RFDs, output from numerical simulations or field observations should be used to determine what refractivity changes would be expected from tornadic and nontornadic RFDs.

1) 8 April 2008

The 8 April 2008 supercell case showed that refractivity data could be used to identify the moisture characteristics of the rear-flank downdraft. The 8 April 2008 supercell had a well-defined hook echo in reflectivity while it passed through the refractivity domain (Fig. 6b). A gust front produced by the rear-flank downdraft was evident in reflectivity as a fine line extending southward from the hook echo and in radial velocity as convergent flow normal to the boundary.

The passage of the gust front associated with the rear-flank downdraft was characterized by a brief increase in dewpoint temperature. As the gust front passed over the Oklahoma City North (OKCN) Mesonet station between 0415 and 0425 UTC, the OKCN station measured an increase in dewpoint temperature of 0.5°C and a refractivity change from 321 to 323 N-units. The scan-to-scan refractivity change at 0428 UTC showed an increase in refractivity between 1 and 3 N-units behind the gust front, with the greatest positive scan-to-scan refractivity changes near the hook echo (Fig. 6a). Scan-to-scan changes of 1 to 3 N-units were also observed behind the gust front as it moved southeastward at 0445, 0502, and 0510 UTC (Fig. 6a). This case illustrated the utility of refractivity data in tracking the position of the gust front in addition to assessing moisture changes caused by the gust front.

2) 2 May 2008

The 2 May 2008 case demonstrated significant potential for refractivity in tornadogenesis forecasting. Refractivity data from the 2 May 2008 case showed near-surface moisture changes within the rear-flank downdraft and the updraft prior to tornadogenesis. As the supercell developed, negative scan-to-scan refractivity changes were observed within the inflow region of the supercell. The first author observed a funnel cloud at 0013 UTC, approximately the same time as the first hook echo was observed in reflectivity on KTLX (Fig. 7b). While the storm was in the refractivity domain, negative scan-to-scan refractivity changes were observed within and east of the hook echo and positive scan-to-scan refractivity changes were observed to the northwest of the hook echo, forming a couplet of positive and negative refractivity changes. Between 0015 and 0029 UTC, the couplet signature moved with the hook echo as the hook echo became more cyclonically curved (Fig. 7a).

Since a classic supercell has the rear-flank downdraft on the upshear side of the hook echo and the updraft region on the downshear side of the hook echo [Bluestein, 1993], the refractivity signature may indicate differences in moisture flux between the rear-flank downdraft and the updraft region. Given the large temperature and pressure perturbations within supercells and the small magnitude of scan-to-scan refractivity changes, temperature or pressure changes may also cause the refractivity changes. The negative scan-to-scan refractivity change in the updraft may also be caused by pressure falls associated with strong upward motion. The supercell produced a very brief tornado 1 mile northwest of Choctaw, Oklahoma at 0029 UTC. By 0040 UTC, the hook echo was no longer observed in reflectivity and the supercell had occluded. A volume scan was missing from the data set between 0028 and 0040 UTC, so the occlusion of the RFD was not seen in radar refractivity.

Based on the conceptual model of the classical supercell, the development of the refractivity gradient between the rear-flank downdraft and the updraft might be a precursor to tornadogenesis. The conceptual model of the classic supercell suggests that a refractivity gradient should be present across the hook echo, at the interface between the updraft and the rear-flank downdraft. The magnitude of the refractivity gradient will be determined by the moisture in the rear-flank downdraft and the moisture of the inflow into the updraft. This case demonstrated that radar refractivity retrievals can show moisture changes associated with the boundary between the rear-flank downdraft and the updraft. Further analysis of field observations or model data will determine if refractivity can be used to discriminate between tornadic and nontornadic supercells.

5. CONCLUSIONS

The presented case studies demonstrate that refractivity could enhance convection initiation forecasts by providing high-resolution moisture data from which boundaries may be identified, and helping users identify boundaries earlier than reflectivity. The 21 April 2008 case showed that refractivity

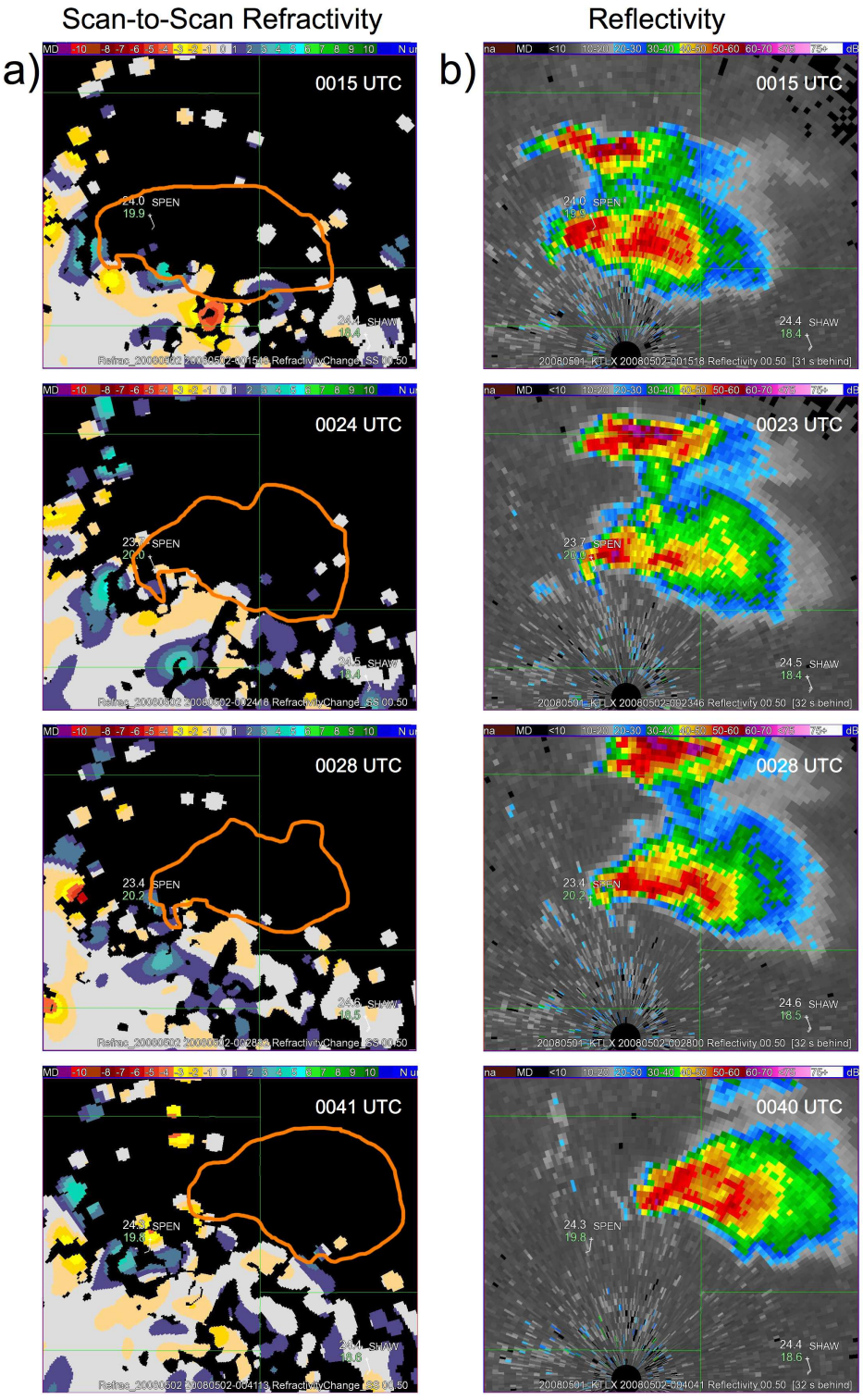

Figure 7: a) Scan-to-scan refractivity change, and b) 0.5°tilt reflectivity at 0015, 0024, 0028, and 0041 UTC 2 May 2008. The orange line shows position of the storm indicated in reflectivity.

data revealed the development of boundaries before fine lines had developed in reflectivity, and could be used to assess the impact of moisture changes on CIN and CAPE for storm initiation forecasts. The 30 April 2007 case showed that refractivity data could identify small-scale moisture perturbations that locally reduce CIN and aid convection initiation. The analysis of more front, boundary, and moisture pool cases may reveal more small-scale structures that are critical to convection initiation.

Refractivity data also showed utility in forecasting storm evolution and resolving small-scale moisture changes within supercells. The 22 April 2008 showed that storm evolution forecasts could be enhanced by monitoring outflow from other storms, which can disrupt the inflow of warm, moist air to other storms. Refractivity data also showed great potential in observing small-scale moisture changes within supercells, which could improve tornadogenesis forecasts. The 8 April 2008 case showed that refractivity data could be used to observe changes in moisture associated with a gust front produced by the rear-flank downdraft. The 2 May 2008 case showed positive and negative scan-to-scan refractivity couplets associated with the rear-flank downdraft and the updraft. The couplet developed simultaneously with the hook echo and preceded a brief tornado.

The refractivity data coverage will expand during the 2008 campaign, with seven radars collecting refractivity data. The refractivity algorithm will be implemented on KFDR (Frederick, Oklahoma), the four CASA X-Band radars [Brotzge et al., 2005], and the NWRT PAR [Zrnić et al., 2007] in addition to KTLX. The seven-radar network will provide nearly continuous refractivity measurements across southwest Oklahoma. The project will continue through 2011 as part of a National Science Foundation grant studying the impact of radar refractivity convection initiation forecasts, storm evolution forecasts, and numerical weather prediction. The expanded domain will significantly increase the number of convection initiation and storm evolution cases observed. Given that convection initiation and storm intensity are sensitive to small-scale moisture changes in the atmosphere, refractivity holds great promise in improving convection initiation and perhaps storm intensity forecasts. Finally, the increased domain size will provide more opportunities to obtain supercell and tornadogenesis cases, and potentially improve tornado warning accuracy and lead-times by helping forecasters discriminate between tornadic and nontornadic supercells.

6. ACKNOWLEDGMENTS

Funding for this research was provided by the Radar Operations Center through grant number NA17RJ1227 and the National Science Foundation through grant number ATM0750790. The first author was supported by an American Meteorological Society Fellowship sponsored by the Raytheon Corporation. The authors would like to thank the Radar Operations Center for maintaining the data flow from KTLX and KFDR during the experiments. The authors would also like to thank Mark Laufersweiler, Kevin Manross, and Travis Smith for their assistance. Finally, the authors would like to thank Paul Markowski for providing the Mobile Mesonet data from VORTEX I.

References

Bean, B. R., and E. J. Dutton, 1968: *Radio Meteorology*. Dover Publications, 435 pp.

Bluestein, H. B., 1993: *Synoptic-Dynamic Meteorology in Midlatitudes*. Vol. 2. Oxford University Press.

Brock, F. V., K. C. Crawford, R. L. Elliott, G. W. Cuperus, S. J. Stadler, H. L. Johnson, and M. D. Eilts, 1995: The Oklahoma Mesonet: A technical overview. *J. Atmos. Oceanic Technol.*, **12**, 5–19.

Brotzge, J. A., K. Brewster, B. Johnson, B. Philips, M. Preston, D. Westbrook, and M. Zink, 2005: CASA's first testbed: Integrated Project #1 (IP1). in *32nd Conf. Radar Meteor.*, CDROM 14R.2, Albuquerque, New Mexico. Amer. Meteor. Soc.

Buban, M., C. Ziegler, E. Rasmussen, and Y. Richardson, 2007: The dryline on 22 may 2002 during ihop: Ground-radar and in situ data analyses of the dryline and boundary layer evolution. *Mon. Wea. Rev.*, **135**, 2473–2505.

Cheong, B. L., R. D. Palmer, C. D. Curtis, T.-Y. Yu, D. S. Zrnić, and D. Forsyth, 2008: Refractivity retrieval using the Phased Array Radar: First results and potential for multi-function operation. *IEEE Tran. Geosci. Remote Sensi.*, **46**, 2527–2537.

Crook, A. N., 1996: Sensitivity of moist convection forced by boundary layer processes to low-level thermodynamic fields. *Mon. Wea. Rev.*, **124**, 1767–1785.

Dabberdt, W. F., and T. W. Schlatter, 1996: Research opportunities from emerging atmospheric observing and modeling capabilities. *Bull. Amer. Meteor. Sci.*, **77**, 305–323.

Demoz, B., C. Flamant, T. Weckwerth, D. Whiteman, K. Evans, F. Fabry, P. Girolamo, D. Miller, B. Geerts, W. Brown, G. Schwemmer, B. Gentry, W. Feltz, and Z. Wang, 2006: The dryline on 22 may 2002 during ihop: Convective-scale measurements at the profiling site. *Mon. Wea. Rev.*, **134**, 294–310.

Emanuel, K., K. D. Raymond, A. Betts, L. Bosart, C. Bretherton, K. Droegemeier, B. Farrell, J. M. Fritsch, R. Houze, M. LeMone, D. Lilly, R. Rotunno, M. Shapiro,

R. Smith, and A. Thorpe, 1995: Report of first prospectus development team of the U.S. weather research program to NOAA and the NSF. *Bull. Amer. Meteor. Sci.*, **76**, 1194–1208.

Fabry, F., 2004: Meteorological value of ground target measurements by radar. *J. Atmos. Oceanic Technol.*, **21**(4), 560–573.

Fabry, F., 2006: The spatial variability of moisture in the boundary layer and its effect on convective initiation: Project-long characterization. *Mon. Wea. Rev.*, **134**, 79–91.

Fabry, F., C. Frush, I. Zawadzki, and A. Kilambi, 1997: On the extraction of near-surface index of refraction using radar phase measurements from ground targets. *J. Atmos. Oceanic Technol.*, **14**(4), 978–987.

Hart, J. A., and W. Korotky, 1991: The sharp workstation vl.50 users guide. Tech. rep., NOAA/National Weather Service, Eastern Region Headquarters, 630 Johnson Ave., Bohemia, NY 11716.

Heinselman, P. L., B. L. Cheong, R. D. Palmer, D. Bodine, and K. Hondl, 2008: Radar refractivity retrievals from ktlx: Insights into operational benefits and limitations. Tech. rep., National Severe Storms Laboratory, 120 David L. Boren Blvd., Suite 4900, Norman, OK 73072.

Koch, S. E., and S. Saleeby, 2001: An automated system for the analysis of gravity waves and other mesoscale phenomena. *Wea. Forecasting*, **16**, 661–679.

Lemon, L. R., and C. A. Doswell III, 1979: Severe thunderstorm evolution and mesocyclone structure as related to tornadogenesis. *Mon. Wea. Rev.*, **107**, 1184–1197.

Markowski, P. M., J. M. Straka, and E. N. Rasmussen, 2002: Direct surface thermodynamic observations within the rear-flank downdraft of nontornadic and tornadic supercells. *Mon. Wea. Rev.*, **130**, 1692–1721.

McPherson, R. A., C. A. Fiebrich, K. C. Crawford, J. R. Kilby, D. L. Grimsley, J. E. Martinez, J. B. Basara, B. G. Illston, D. A. Morris, K. A. Kloesel, A. D. Melvin, H. Shrivastava, J. M. Wolfinbarger, J. P. Bostic, and D. B. Demko, 2007: Statewide monitoring of the mesoscale environment: A technical update on the oklahoma mesonet. *J. Atmos. Oceanic Technol.*, **24**, 301–321.

National Research Council, 1998: *The Atmospheric Sciences: Entering the Twenty-First Century*. National Academy Press.

Parsons, D. B., M. A. Shapiro, and E. Miller, 2000: The mesoscale structure of a nocturnal dryline and of a frontal-dryline merger. *Mon. Wea. Rev.*, **128**, 3824–3838.

Roberts, R. D., F. Fabry, P. C. Kennedy, E. Nelson, J. Wilson, N. Rehak, J. Fritz, V. Chandrasekar, J. Braun, J. Sun, S. Ellis, S. Reising, T. Crum, L. Mooney, R. Palmer, T. Weckwerth, and S. Padmanabhan, 2008: Refractt-2006: Real-time retrieval of high-resolution low-level moisture fields from operational nexrad and research radars. *Bull. Amer. Meteor. Sci.*, **in press**.

Weckwerth, T. M., C. R. Pettet, F. Fabry, S. Park, M. A. LeMone, and J. W. Wilson, 2005: Radar refractivity retrieval: Validation and application to short-term forecasting. *J. Appl. Meteorol.*, **44**(3), 285–300.

Wilson, J. W., and W. E. Schreiber, 1986: Initiation of convective storms at radar-observed boundary-layer convergence lines. *Mon. Wea. Rev.*, **114**, 2516–2536.

Ziegler, C. L., T. J. Lee, and R. A. P. Sr., 1996: Convective initiation at the dryline: A modeling study. *Mon. Wea. Rev.*, **125**, 1001–1026.

Ziegler, C. L., and E. N. Rasmussen, 1998: The initiation of moist convection at the dryline: forecasting issues from a case study perspective. *Wea. Forecasting*, **13**, 1106–1131.

Zrnić, D. S., J. F. Kimpel, D. E. Forsyth, A. Shapiro, G. Crain, R. Ferek, J. Heimmer, W. Benner, T. J. McNellis, and R. J. Vogt, 2007: Agile-beam phased array radar for weather observations. *Bull. Amer. Meteor. Sci.*, **88**, 1753–1766.